Density Functional Calculations of Native Defects in CH 3 NH 3 PbI 3 : Effects of Spin−Orbit Coupling and Self−Interaction Error

1 AUTHOR:

Mao-Hua Du

Oak Ridge National Laboratory

119 PUBLICATIONS **4,836** CITATIONS

Density Functional Calculations of Native Defects in CH₃NH₃PbI₃: Effects of Spin−Orbit Coupling and Self-Interaction Error

Mao-Hua Du*

Materials Science & Technology Division, Oak Ridge National Laboratory, Oak Ridge, Tennessee 37831, United States

ABSTRACT: Native point defects play an important role in carrier transport properties of CH₃NH₃PbI₃. However, the nature of many important defects remains controversial due partly to the conflicting results reported by recent density functional theory (DFT) calculations. In this Letter, we show that self-interaction error and the neglect of spin−orbit coupling (SOC) in many previous DFT calculations resulted in incorrect positions of valence and conduction band edges, although their difference, which is the band gap, is in good agreement with the experimental value. This problem has led to incorrect predictions of defect-level positions. Hybrid density functional calculations, which partially correct the self-interaction error and include the SOC, show that, among native point defects (including vacancies, interstitials, and antisites), only the iodine vacancy and its complexes induce deep electron and hole trapping levels inside of the band gap, acting as nonradiative recombination centers.
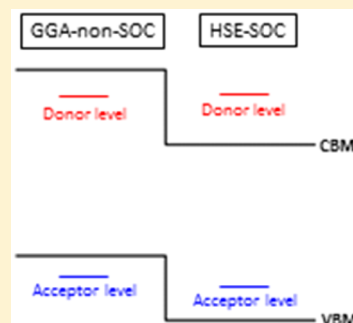
Methylammonium (MA) lead iodide (CH₃NH₃PbI₃) and related halide perovskites (e.g., CH₃NH₃PbI₃₋ₓClₓ) have recently emerged as promising photovoltaic materials.[1] One of the attractive properties of these halide perovskites is efficient carrier transport, manifested by good carrier mobility, long carrier lifetime, and long carrier diffusion length.[2−6] Defects play important roles in carrier transport in semiconductors. In particular, deep defect centers are carrier traps and nonradiative recombination centers, which are detrimental to carrier transport. Therefore, understanding defect properties is extremely important for optimizing the performance of halide perovskite solar cells.

A large number of native point defects (including vacancies, interstitials, and antisites) and defect complexes (Schottky defect and Frenkel defect) have been studied by density functional theory (DFT) calculations.[7−11] However, these calculations have shown conflicting results on the positions of many native defect levels in CH₃NH₃PbI₃. The main issue under debate is whether or not several important native defects introduce deep charge transition levels in the band gap of CH₃NH₃PbI₃. These defects are the iodine vacancy (V_I), iodine interstitial (I_i), Pb interstitial (Pb_i), and two antisites (I_{MA} and Pb_{MA}). V_I was predicted to be a shallow donor by refs 7, 8, 10, and 11 but was shown to be an amphoteric defect with a deep (+/−) transition level in the band gap in ref 9. I_i was shown to be a shallow acceptor in refs 7 and 9. In contrast, ref 8 showed that I_i is a deep carrier trap and nonradiative recombination center. The Pb_i double electron donor was shown to be deep in refs 7 and 9 but shallow in ref 8. I_{MA} and Pb_{MA} are essentially I_i and Pb_i, respectively, complexed with a shallow acceptor V_{MA}.[8,9] Therefore, the discrepancies in I_i and Pb_i also exist in I_{MA} and Pb_{MA}. All other native defects have been shown to be shallow defects by previous DFT calculations.[7−11]

Serious discrepancies in calculated defect levels of CH₃NH₃PbI₃ in the literature suggest that a reexamination of the computational methods and defect structures is urgently needed. These discrepancies need to be understood and resolved before reliable computational results on other related systems (such as grain boundaries and dopants in CH₃NH₃PbI₃ as well as defects in other halide perovskites) can be obtained.

The different defect structures optimized by different authors should contribute to the aforementioned discrepancies in defect levels in CH₃NH₃PbI₃. Reference 8 showed an I_i structure that has not been reported elsewhere. Reference 9 reported new I_{MA} and Pb_i structures. Different phases of CH₃NH₃PbI₃ (i.e., α-CH₃NH₃PbI₃,[7] β-CH₃NH₃PbI₃,[8,9,11] and γ-CH₃NH₃PbI₃[10]) used in defect calculations may also contribute to the different defect levels. In this Letter, we discuss the defect structures in β-CH₃NH₃PbI₃ (the room-temperature phase of CH₃NH₃PbI₃). Importantly, we show that DFT calculations that neglect spin−orbit coupling (SOC) and use local density approximation (LDA) or generalized gradient approximation (GGA) misplace the positions of both the conduction band minimum (CBM) and the valence band maximum (VBM) despite predicting a correct band gap. Such a computational method, which was employed in many previous defect calculations (e.g., refs 7, 9, and 10), can result in qualitative errors in the predicted defect-level positions, especially in deep levels.

There are mainly two computational methods that have previously been used for defect calculations in CH₃NH₃PbI₃, that is, GGA calculations without SOC[7,9,10] and hybrid functional calculations with SOC.[8,11] LDA and GGA calculations typically underestimate band gaps. This is partially due to the self-interaction error, which raises the VBM. We find that the GGA band gap of β-CH₃NH₃PbI₃ is 0.60 eV, whereas

the experimental band gap is 1.51 eV.[12,13] The SOC effect is important in the electronic structure of $CH_3NH_3PbI_3$ due to the heavy Pb and I elements.[14−17] Neglecting the SOC raises the CBM by 0.81 eV and lowers the VBM by 0.17 eV, thereby increasing the band gap to 1.59 eV, which is in good agreement with the experimental value. Hence, many previous calculations neglected the SOC for obtaining the correct band gap as well as for reducing computational time.[7,9,10] However, this is a correction of the band gap based on error cancellation.[18] Both the CBM and the VBM are in fact artificially high due to the absence of the SOC and the self-interaction error of GGA, respectively, although their difference, which is the band gap, is in good agreement with the experimental value.

On the other hand, a hybrid density functional calculation incorporating a fraction (α) of Fock exchange[19,20] partially removes the self-interaction error, thereby lowering the VBM substantially relative to that of a GGA calculation. Hybrid functional calculations have recently been applied to many semiconductors and have generally shown improvement in calculated structural, electronic, dielectric, and defect proper-ties.[21−29] A band gap of 1.50 eV is obtained for β-$CH_3NH_3PbI_3$ by using Heyd−Scuseria−Ernzerhof (HSE) hybrid func-tionals[19,20] (α = 0.43) including SOC.[8] The band gap correction in a hybrid functional calculation is mostly attributed to the lowering of the VBM, which is important for predicting defect properties. For example, the existence of AX centers in several p-doped II−VI semiconductors was correctly predicted by hybrid functional calculations but was shown to be unstable by LDA and GGA calculations due to the artificially high VBM obtained by LDA and GGA calculations.[28]

Although the GGA-non-SOC and the HSE-SOC calculations both give a good band gap of $CH_3NH_3PbI_3$, the differences in the positions of the CBM and the VBM between these two calculations lead to drastically different predictions of defect level positions. Figure 1 shows a schematic that illustrates two cases in which qualitatively different results in defect levels are obtained by GGA-non-SOC and HSE-SOC calculations. In Figure 1, the electron trapping level, the (+/0) level, of the donor defect, D, is deep in GGA calculations but shallow in HSE calculations mainly because the former neglects the SOC whereas the latter includes it. On the other hand, the hole trapping level, the (0/−) level, of an acceptor defect, A, is shallow in GGA calculations but deep in HSE calculations due to the self-interaction error in GGA, which raises the VBM and consequently lowers the energy of a free hole relative to a trapped hole. The failure of GGA calculations to predict the deep (+/−) transition for the defect A in Figure 1 is analogous to the failure to predict the stability of AX centers in II−VI semiconductors.[28]

Figure 2 shows calculated charge transition levels for V_I, I_i, I_{MA}, Pb_i, and Pb_{MA} in β-$CH_3NH_3PbI_3$ using GGA-non-SOC,[31] GGA-SOC, and HSE-SOC (α = 0.43) calculations. The band edges in different calculations were referenced to the common average potential in the supercell. Because the HSE calculations are very time-consuming, the defect structures optimized using GGA-SOC calculations were used in HSE calculations.

The electron−ion interactions were described using projector-augmented wave potentials.[32] The numbers of valence electrons for Pb, I, C, N, and H that were included in the calculations are 14, 7, 4, 5, and 1, respectively. The valence wave functions were expanded in a plane wave basis with a cutoff energy of 400 eV. All atoms were relaxed to minimize the Feynman−Hellmann forces to below 0.05 eV/Å.
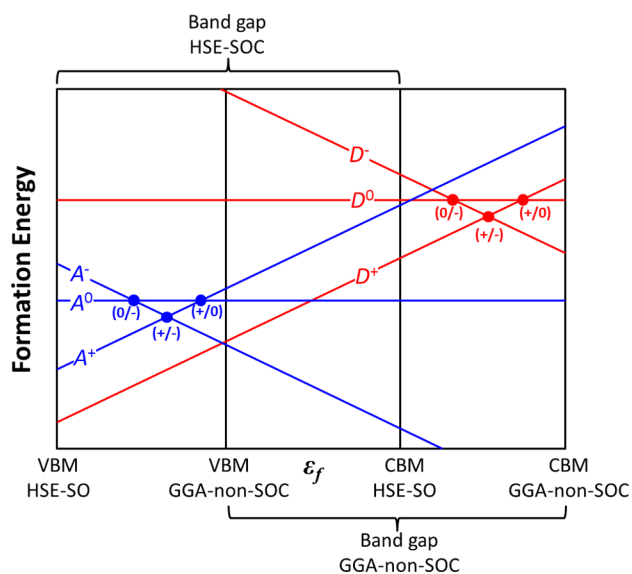

Figure 1. A schematic of formation energies of a single-electron donor (D) and a single-electron acceptor (A) as a function of Fermi level (ε_f) in $CH_3NH_3PbI_3$. The VBM and the CBM calculated using GGA-non-SOC and HSE-SOC calculations are shown. The defect formation energy is a function of the Fermi level[30] ($\Delta H_f = A + q\varepsilon_f$, where q is the charge state of the defect and A is arbitrary for the schematic figure shown here). The slope of a formation energy line indicates the charge state of the defect. The Fermi level at which the formation energy lines for two different charge states of a defect intersect is the charge transition level.

A 2 × 2 × 1 tetragonal supercell containing 16 formula units of $CH_3NH_3PbI_3$ was used to study native point defects in β-$CH_3NH_3PbI_3$. A 1 × 1 × 2 grid was used for k-point sampling of the Brillouin zone. Using a 2 × 2 × 2 grid results in small changes in charge transition levels (well below 0.1 eV) in tests done on an iodine vacancy. The charge transition level $\varepsilon(q/q')$ for a defect is determined by the Fermi level (ε_f), at which the formation energies of the defect with charge states q and q' are equal to each other.[30] $\varepsilon(q/q')$ can be calculated using

$$\varepsilon(q/q') = \frac{E_{D,q'} - E_{D,q}}{q - q'} \tag{1}$$

where $E_{D,q}(E_{D,q'})$ is the total energy of the supercell that contains the relaxed structure of a defect at charge state q (q'). More computational details have been published elsewhere.[8] All calculations were performed using the VASP codes.[33,34]

Experimental lattice parameters for $CH_3NH_3PbI_3$ were used in all calculations (tetragonal: a = 8.849 Å, c = 12.642 Å)[12] Using experimentally measured or theoretically optimized lattice constant usually makes negligible differences in calculated defect transition levels because the difference in the calculated total energies caused by using slightly different lattice constants is largely canceled out when evaluating the total energy difference in eq 1.

We focus on charge trapping at localized defect states with substantial local structural relaxation because such local trapping may lead to deep charge trapping. The charge transition levels shown in Figure 2 all correspond to the local charge trapping (within the length scale of the lattice constant). Shallow hydrogenic levels, which are close to the CBM or the VBM and correspond to charge trapping by long-range Coulomb attraction with negligible structural relaxation, are
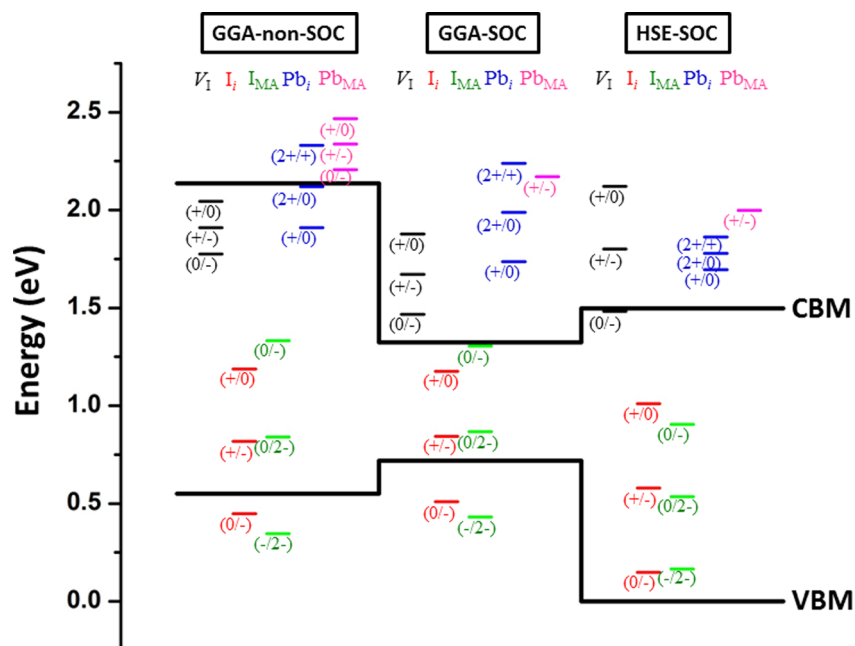
Figure 2. Charge transition levels of V_I, I_i, I_{MA}, Pb_i, and Pb_{MA} in β-CH$_3$NH$_3$PbI$_3$ calculated using GGA-non-SOC, GGA-SOC, and HSE-SOC (α = 0.43) calculations. For Pb_{MA}, only the $(+/-)$ level is shown when the SOC is included because a localized Pb_{MA}^0 cannot be stabilized when the SOC is included. See the text for details.
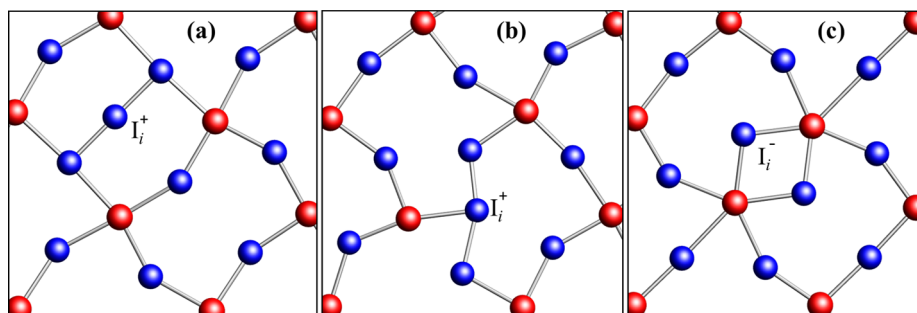

Figure 3. Two I_i^+ structures (a,b) and the structure of I_i^- (c). Only one Pb–I layer (parallel to the *ab* plane) is shown for clarity. Red and blue balls represent Pb and I atoms, respectively.

not calculated. The strong structural relaxation upon charge trapping leads to the negative-U behavior. Take I_i as an example, its $(+/0)$ level is higher than its $(0/-)$ level (see also a schematic of formation energies in Figure 1), indicating strong structural relaxation upon electron trapping at the defect. The neutral charge state of I_i is metastable. The $(+/-)$ level determines the charge transition between the two stable charge states, that is, $+1$ and -1. The $(+/0)$ level is the electron trapping level for I_i^+, while the $(0/-)$ level is the hole trapping level for I_i^-.

Note that a thermodynamic charge transition level for a defect, which is calculated based on the total energy difference between two charge states associated with two different defect structures (eq 1),[30] is different from a defect-induced single-particle level, which is obtained by solving single-particle Kohn−Sham equations[35] for a fixed structure. As mentioned above, we considered only local charge trapping at defects, for which the charge is always trapped at a defect-induced single-particle level deep inside of the band gap. However, a thermodynamic charge transition level of a defect can be outside of the band gap, such as the $(+/0)$ level for V_I and the $(2+/+)$ level for Pb_i calculated with SOC (see Figure 2). In

these cases, the lowering of the energy due to the charge trapping at the single-particle defect level inside of the band gap is less than the energy penalty brought by charge-localization-induced structural distortion; consequently, the local charge trapping associated with strong structural relaxation is metastable, and a charge carrier would prefer to be trapped by a shallow hydrogenic level.

The general trends in Figure 2 are that (1) some defect levels are below the CBM in GGA-non-SOC calculations (e.g., those of V_I) but are above the CBM after including the SOC because the SOC lowers the CBM substantially and (2) some acceptor levels are below the VBM in GGA calculations [e.g., the $(0/-)$ level of I_i] but are inside of the band gap in HSE calculations due to the reduction of the self-interaction error that lowers the VBM substantially. In HSE-SOC calculations, V_I, Pb_i, and Pb_{MA} are shallow donors, introducing only shallow hydrogenic levels below the CBM.

I_i and I_{MA} can each assume two different stable charge states. I_i^+ and I_{MA}^0 are stable when the Fermi level is low, while I_i^- and I_{MA}^{2-} are stable when the Fermi level is high. Because I_{MA} is a complex of I_i and V_{MA}, the defect levels of I_i and I_{MA} are close to each other. The HSE-SOC calculations show that the $(+/-)$

and the (0/2−) transition levels for I_i and I_{MA} are 0.57 and 0.54 eV above the VBM, respectively, as shown in Figure 2. The Fermi levels in $CH_3NH_3PbI_3$ were shown to be either near midgap in planar thin-film device architectures or near the CBM in meso-superstructured device architectures.[36] Under these conditions, I_i^- and I_{MA}^{2-} are stable, and their acceptor levels are deep, that is, the (0/−) level for I_i and the (−/2−) level for I_{MA} are 0.15 and 0.17 eV above the VBM, respectively. These calculated deep acceptor level positions of I_i and I_{MA} are close to an observed defect level ~0.16 eV above the VBM measured using admittance spectroscopy.[37] Our calculations further show that neither I_i^- nor I_{MA}^{2-} have single-particle levels inside of the band gap, although their thermodynamic hole trapping levels are inside of the band gap. Therefore, I_i^- and I_{MA}^{2-} cannot be excited by sub-band-gap excitation and cannot be easily seen in optical absorption experiments.[38]

The HSE-SOC calculations predict that, among native point defects (vacancies, interstitials, antisites, and their complexes), only I_i and its complexes (such as I_{MA}) introduce deep levels inside of the band gap of β-$CH_3NH_3PbI_3$. Other native point defects are shallow. These results agree with those in ref 8, in which the HSE-SOC calculations were also used. Next, we briefly discuss the defect structures upon which the results in Figure 2 are based.

I_i and I_{MA}: I_i^- is a split interstitial (see Figure 3c), where two iodine ions occupy the same iodine site. The structure of I_i^- shown in Figure 3c has two I^- ions lying on the ab plane, each of which binds two Pb ions. This structure is slightly more stable than that shown in ref 8, where the two I^- ions are not on the ab plane. I_i^+ prefers to be coordinated with two other iodine ions on the ab plane in triplet structures shown in Figure 3a and b. The structure in Figure 3a is new, while that in Figure 3b is similar to that reported in ref 8. The energies of these two structures differ by less than 0.01 eV at the GGA-SO level. In the iodine triplets in Figure 3a and b, the interstitial iodine ion in the middle is positively charged, whereas the two other iodine ions are negatively charged. Such an iodine triplet structure for I_i^+ is similar to the bromine triplet structure for Br_i^+ in TlBr.[39] I_{MA} can be considered as a complex of I_i and V_{MA} (see Figure 4). I_{MA}^0 also features an iodine triplet, in which I_i^+ is
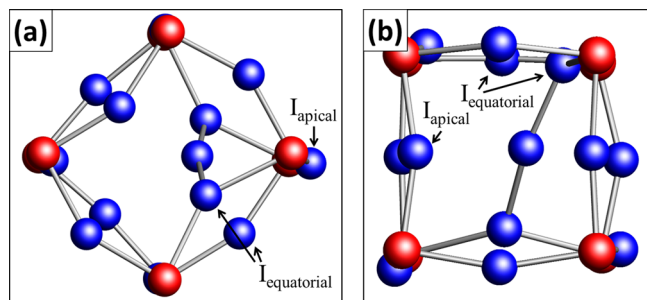

Figure 4. Structures of I_{MA}^0 viewed from (a) the [001] and the [110] directions. I_{MA}^0 can be viewed as a complex of I_i^+ (an iodine triplet) and V_{MA}^-. Red and blue balls represent Pb and I atoms, respectively.

coordinated with two equatorial iodine ions on two adjacent Pb−I layers (both parallel to the ab plane), consistent with the structure predicted in ref 9. The structure of I_i^- in I_{MA}^{2-} is similar to that of an isolated I_i^- (see Figure 3c) except that the two iodine ions occupying the same iodine site align along the c axis instead of lying on the ab plane.

Pb_i and Pb_{MA}: The structure of Pb_i^{2+} is shown in Figure 5a, in which the Pb_i ion binds with four equatorial I^- ions on the ab
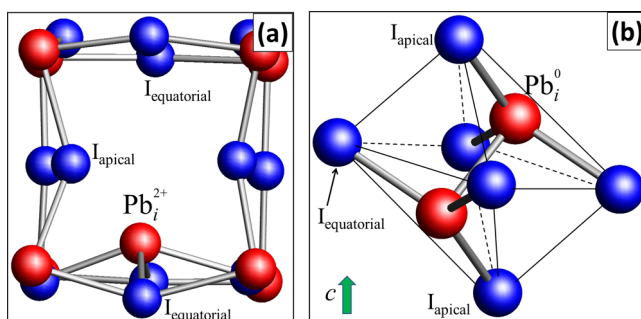

Figure 5. Structures of (a) Pb_i^{2+} and (b) Pb_i^0. The CH_3NH_3 cations are not shown for clarity. Red and blue balls represent Pb and I atoms, respectively.

plane and also strongly attracts two nearby apical I^- ions, causing significant displacements of the two apical I^- ions, as can be seen in Figure 5a. This structure is clearly dictated by the Coulomb attraction between Pb_i^{2+} and surrounding I^- ions. For Pb_i^0, the electrostatic interaction between the interstitial Pb and the surrounding ions is much reduced. The structure of Pb_i^0 prefers a split interstitial, in which a pair of Pb occupies one Pb site with a Pb−Pb bond formed. However, Pb_i^0 is metastable because the (2+/0) transition level of Pb_i is above the CBM. It is energetically favorable for Pb_i^0 to release its two bound electrons to the conduction band (becoming free electrons), leaving Pb_i^{2+} to make ionic bonds with I^- ions. Therefore, Pb_i is a shallow double electron donor. Clearly, ionicity plays a dominant role over covalency in determining the structure and the charge state of Pb_i. Pb_{MA} is a complex of Pb_i and V_{MA} and is a shallow single-electron donor. Note that only the (+/−) level for Pb_{MA} is shown in Figure 2 when the SOC is included because a localized Pb_{MA}^0 cannot be stabilized in the calculations including the SOC. Pb_{MA}^0 induces a deep single-particle defect level, which is an unpaired electron level, inside of the band gap if the SOC is neglected. This defect level, however, is above the CBM if the SOC is included. Therefore, the inclusion of SOC releases the electron from the local defect state to the delocalized bulk state at CBM, effectively resulting in a Pb_{MA}^+ and a free electron. The addition of one electron to Pb_{MA}^0 forming Pb_{MA}^- causes strong structural relaxation that pushes the single-particle defect level (fully occupied) below the CBM even if the SOC is included. Thus, Pb_{MA}^- can be stabilized in the calculations including the SOC but Pb_{MA}^0 cannot.

V_I: Similar to Pb_i, V_I is a shallow donor. V_I^- with two electrons trapped on a bound state forming a Pb−Pb bond is metastable because the (+/−) level is above the CBM. The calculated structure of V_I^- is consistent with that shown in ref 9. Similar defect structures have also been reported for V_{Br} in $CsPbBr_3$.[11] However, for V_{Br} in $CsPbBr_3$, the (+/−) level is below the CBM due to a shorter Pb−Pb bond in a smaller Br vacancy.

In summary, we show that although the band gaps of $CH_3NH_3PbI_3$ predicted by GGA-non-SOC and HSE-SOC calculations are both in good agreement with the experimental value, the VBM and the CBM obtained by these two calculations are drastically different. The prediction of many deep defect levels near the CBM and the failure to predict the deep acceptor levels near the VBM in GGA-non-SOC calculations are the artifacts arising from the neglect of SOC

(which raises the CBM) and from large self-interaction error (which raises the VBM), respectively. The HSE-SOC calculations that remove these two artifacts show that, among native point defects (including vacancies, interstitials, and antisites), only the iodine interstitial and its complexes (such as a complex of iodine interstitial and MA vacancy) can introduce deep electron and deep hole trapping levels in the band gap, thereby acting as nonradiative recombination centers. This study resolves the conflicting reports on native defect properties in $CH_3NH_3PbI_3$ and paves the way for future studies of defects and dopants in various halide perovskite solar materials.

■ AUTHOR INFORMATION

Corresponding Author
*E-mail: mhdu@ornl.gov.

Notes
The authors declare no competing financial interest.

■ ACKNOWLEDGMENTS

■ REFERENCES

(1) Green, M. A.; Ho-Baillie, A.; Snaith, H. J. The Emergence of Perovskite Solar Cells. *Nat. Photonics* **2014**, *8*, 506−514.

(2) Dong, Q.; Fang, Y.; Shao, Y.; Mulligan, P.; Qiu, J.; Cao, L.; Huang, J. Electron−Hole Diffusion Lengths > 175 μm in Solution-Grown Single Crystals. *Science* **2015**, *347*, 967−970.

(3) Stranks, S. D.; Eperon, D. E.; Grancini, G.; Menelaou, C.; Alcocer, M. J.; Leijtens, T.; Herz, L. M.; Petrozza, A.; Snaith, H. J. Electron−Hole Diffusion lengths Exceeding 1 Micrometer in an Organometal Trihalide Perovskite Absorber. *Science* **2013**, *342*, 341−344.

(4) Xing, G.; Mathews, N.; Sun, S.; Lim, S. S.; Lam, Y. M.; Grätzel, M.; Mhaisalkar, S.; Sum, T. C. Long-Range Balanced Electron- and Hole-Transport Lengths in Organic−Inorganic $CH_3NH_3PbI_3$. *Science* **2013**, *342*, 344−347.

(5) Wehrenfennig, C.; Eperon, G. E.; Johnston, M. B.; Snaith, H. J.; Herz, L. M. High Charge Carrier Mobilities and Lifetimes in Organolead Trihalide Perovskite. *Adv. Mater.* **2014**, *26*, 1584−1589.

(6) Takahashi, Y.; Hasegawa, H.; Takahashi, Y.; Inabe, T. Hall Mobility in Tin Iodide Perovskite $CH_3NH_3PbI_3$: Evidence for a Doped Semiconductor. *J. Solid State Chem.* **2013**, *205*, 39−43.

(7) Yin, W. J.; Shi, T.; Yan, Y. F. Unusual Defect Physics in $CH_3NH_3PbI_3$ Perovskite Solar Cell Absorber. *Appl. Phys. Lett.* **2014**, *104*, 063903.

(8) Du, M. H. Efficient Carrier Transport in Halide Perovskites: Theoretical Perspectives. *J. Mater. Chem. A* **2014**, *2*, 9091−9098.

(9) Agiorgousis, M. L.; Sun, Y. Y.; Zeng, H.; Zhang, S. B. Strong Covalency-Induced Recombination Centers in Perovskite Solar Cell Material $CH_3NH_3PbI_3$. *J. Am. Chem. Soc.* **2014**, *136*, 14570−14575.

(10) Kim, J.; Lee, S. H.; Lee, J. H.; Hong, K. H. The Role of Intrinsic Defects in Methylammonium Lead Iodide Perovskite. *J. Phys. Chem. Lett.* **2014**, *5*, 1312−1317.

(11) Shi, H.; Du, M. H. Shallow Halogen Vacancies in Halide Optoelectronic Materials. *Phys. Rev. B* **2014**, *90*, 174103.

(12) Stoumpos, C. C.; Malliakas, C. D.; Kanatzidis, M. G. Semiconducting Tin and Lead Iodide Perovskites with Organic Cations: Phase Transitions, High Mobilities, and Near-Infrared Photoluminescent Properties. *Inorg. Chem.* **2013**, *52*, 9019−9038.

(13) Baikie, T.; Fang, Y.; Kadro, J. M.; Schreyer, M.; Wei, F.; Mhaisalkar, S. G.; Grätzel, M.; White, T. J. Synthesis and Crystal Chemistry of the Hybrid Perovskite $(CH_3NH_3)PbI_3$ for Solid-State Sensitised Solar Cell Applications. *J. Mater. Chem. A* **2013**, *1*, 5628−5641.

(14) Even, J.; Pedesseau, L.; Jancu, J.-M.; Katan, C. Importance of Spin−Orbit Coupling in Hybrid Organic/Inorganic Perovskites for Photovoltaic Applications. *J. Phys. Chem. Lett.* **2013**, *4*, 2999.

(15) Umari, P.; Mosconi, E.; De Angelis, F. Relativistic GW Calculations on $CH_3NH_3PbI_3$ and $CH_3NH_3SnI_3$ Perovskites for Solar Cell Applications. *Sci. Rep.* **2014**, *4*, 4467.

(16) Menéndez-Proupin, E.; Palacios, P.; Wahnón, P.; Conesa, J. C. Self-Consistent Relativistic Band Structure of the $CH_3NH_3PbI_3$ Perovskite. *Phys. Rev. B* **2014**, *90*, 045207.

(17) Brivio, F.; Butler, K. T.; Walsh, A.; van Schilfgaarde, M. Relativistic Quasiparticle Self-Consistent Electronic Structure of Hybrid Halide Perovskite Photovoltaic Absorbers. *Phys. Rev. B* **2014**, *89*, 155204.

(18) Mosconi, E.; Amat, A.; Nazeeruddin, M. K.; Grätzel, M.; De Angelis, F. First Principles Modeling of Mixed Halide Organometal Perovskites for Photovoltaic Applications. *J. Phys. Chem. C* **2013**, *117*, 13902−13913.

(19) Heyd, J.; Scuseria, G. E.; Ernzerhof, M. Hybrid Functionals Based on a Screened Coulomb Potential. *J. Chem. Phys.* **2003**, *118*, 8207.

(20) Krukau, A. V.; Vydrov, O. A.; Izmaylov, A. F.; Scuseria, G. E. *J. Chem. Phys.* **2006**, *125*, 224106.

(21) Paier, J.; Marsman, M.; Hummer, K.; Kresse, G.; Gerber, I. C.; Angyan, J. G. Screened Hybrid Density Functionals Applied to Solids. *J. Chem. Phys.* **2006**, *124*, 154709.

(22) Muñoz Ramo, D.; Shluger, A. L.; Gavartin, J. L.; Bersuker, G. *Phys. Rev. Lett.* **2007**, *99*, 155504.

(23) Muñoz Ramo, D.; Gavartin, J. L.; Shluger, A. L.; Bersuker, G. Theoretical Prediction of Intrinsic Self-Trapping of Electrons and Holes in Monoclinic HfO_2. *Phys. Rev. B* **2007**, *75*, 205336.

(24) Alkauskas, A.; Broqvist, P.; Pasquarello, A. Defect Energy Levels in Density Functional Calculations: Alignment and Band Gap Problem. *Phys. Rev. Lett.* **2008**, *101*, 046405.

(25) Alkauskas, A.; Broqvist, P.; Devynck, F.; Pasquarello, A. Band Offsets at Semiconductor−Oxide Interfaces from Hybrid Density-Functional Calculations. *Phys. Rev. Lett.* **2008**, *101*, 106802.

(26) Du, M. H.; Zhang, S. B. Impurity-Bound Small Polarons in ZnO: Hybrid Density Functional Calculations. *Phys. Rev. B* **2009**, *80*, 115217.

(27) Janotti, A.; Varley, J. B.; Rinke, P.; Umezawa, N.; Kresse, G.; Van de Walle, C. G. Hybrid Functional Studies of the Oxygen Vacancy in TiO_2. *Phys. Rev. B* **2010**, *81*, 085212.

(28) Biswas, K.; Du, M. H. AX Centers in II−VI Semiconductors: Hybrid Functional Calculations. *Appl. Phys. Lett.* **2011**, *98*, 181913.

(29) Komsa, H.-P.; Broqvist, P.; Pasquarello, A. Alignment of Defect Levels and Band Edges Through Hybrid Functionals: Effect of Screening in the Exchange Term. *Phys. Rev. B* **2010**, *81*, 205118.

(30) Van de Walle, C. G.; Neugebauer, J. First-Principles Calculations for Defects and Impurities: Applications to III-Nitrides. *J. Appl. Phys.* **2004**, *95*, 3851−3879.

(31) Perdew, J. P.; Burke, K.; Ernzerhof, M. Generalized Gradient Approximation Made Simple. *Phys. Rev. Lett.* **1996**, *77*, 3865.

(32) Blöchl, P. E. Projector Augmented-Wave Method. *Phys. Rev. B* **1994**, *50*, 17953.

(33) Kresse, G.; Furthmüller, J. Efficient Iterative Schemes for Ab Initio Total-Energy Calculations Using a Plane-Wave Basis Set. *Phys. Rev. B* **1996**, *54*, 11169.

(34) Kresse, G.; Joubert, D. From Ultrasoft Pseudopotentials to the Projector Augmented-Wave Method. *Phys. Rev. B* **1999**, *59*, 1758.

(35) Kohn, W.; Sham, L. J. Self-Consistent Equations Including Exhange and Correlation Effects. *Phys. Rev.* **1965**, *140*, A1133−A1138.

(36) Leijtens, T.; Stranks, S. D.; Eperon, G. E.; Lindblad, R.; Johansson, E. M. J.; McPherson, I. J.; Rensmo, H.; Ball, J. M.; Lee, M. M.; Snaith, H. J. Electronic Properties of Meso-Superstructured and Planar Organometal Halide Perovskite Films: Charge Trapping, Photodoping, and Carrier Mobility. *ACS Nano* **2014**, *8*, 7147−7155.

(37) Duan, H.-S.; Zhou, H.; Chen, Q.; Sun, P.; Luo, S.; Song, T. −B; Bob, B.; Yang, Y. The Identification and Characterization of Defect States in Hybrid Organic−Inorganic Perovskite Photovoltaics. *Phys. Chem. Chem. Phys.* **2015**, *17*, 112−116.

(38) De Wolf, S.; Holovsky, J.; Moon, S.-J.; Löper, P.; Niesen, B.; Ledinsky, M.; Haug, F.-J.; Yum, J.-H.; Ballif, C. Organometallic Halide Perovskites: Sharp Optical Absorption Edge and Its Relation to Photovoltaic Performance. *J. Phys. Chem. Lett.* **2014**, *5*, 1035−1039.

(39) Du, M. H. First-Principles Study of Native Defects in TlBr: Carrier Trapping, Compensation, and Polarization Phenomenon. *J. Appl. Phys.* **2010**, *108*, 053506.